Control Engineering Practice 158 (2025) 106274

Contents lists available at ScienceDirect

Control Engineering Practice

journal homepage: www.elsevier.com/locate/conengprac

Switched control barrier functions-based safe docking control strategy for a planar floating platform

Akshit Saradagi *, Viswa Narayanan Sankaranarayanan, Avijit Banerjee, Sumeet Satpute, George Nikolakopoulos

Robotics and Artificial Intelligence Group, Department of Computer Science, Electrical and Space Engineering, Lulea University of Technology, Lulea, SE-97187, Norrbotten, Sweden

ARTICLE INFO

Keywords:
Control barrier functions
Autonomous docking
Planar floating platforms
Safety critical systems
Space-emulating test-beds
Control applications
Robotics

ABSTRACT

In this article, we present and experimentally validate a safe docking control strategy designed for an experimental planar floating platform, called the Slider. Three degrees-of-freedom (DOF) platforms like the Slider are used extensively in space industry and academia to emulate micro-gravity conditions on Earth, for validating in-plane Guidance, Navigation and Control (GNC) algorithms. The Slider uses an air cushion (induced by air bearings) to levitate on a smooth flat table, thus emulating the in-plane zero-gravity motion of a spacecraft in orbit. The proposed docking control strategy is applicable in the in-plane approach and docking phases of space docking missions, and is based on the Control Barrier Functions (CBF) approach, where a safe set (a Cardioid), capturing the clearance and direction-of-approach constraints, is rendered positively forward invariant. To enable precise and safe docking in the presence of unmodeled dynamics, disturbances induced by the tether and drifts induced by the non-flat floating surface, we present a switching strategy among the zero and positive level sets of a Cardioid function. In the approach phase, the positive contour of the Cardioid function smoothly steers the Slider platform into the neighborhood of a deadlock point, which is designed to be at a safe distance from the docking port. In the neighborhood of the deadlock point, Slider corrects its proximity and heading until its configuration is well-suited to enter the docking phase. The docking maneuver is initiated by the CBF switching mechanism (positive to zero contour), which expands the safe zone to include the final docking configuration. We present an analysis of the Quadratic program defining the CBF filter, and identify two deadlock points (an asymptotically stable point in the vicinity of the docking port and an unstable point diametrically opposite on the CBF boundary). Both the approach and docking phases are validated through experimentation on the Slider platform, in the presence of tether-induced disturbances and drifts induced by the non-ideal floating surface. In the docking phase, the CBF switching condition effectively handles experimental non-idealities and recovers the slider platform from unsafe configurations. The proposed docking strategy caters to the in-plane (3DOF) approach and docking phases of real space docking missions and is scalable to three-dimensional 6DOF operations, in conjunction with controllers that stabilize the attitude and the out-of-plane degree-of-freedom. Link to the video of experimental demonstration: https://youtu.be/eBiWvnKtG7U?si=QFPD-vm11wydyZSd.

1. Introduction

Due to the remarkable growth experienced by the space industry in the recent years, the topic of sustainable use of outer space is in the spotlight. As a result, the space research community is moving towards sustainable missions like spacecraft refueling (Barbara, Lizy-Destrez, Guardabasso, & Alary, 2020), on-orbit servicing (Li et al., 2019), in-space manufacturing and assembly (Roa Garzon, Nottensteiner, Wedler, & Grunwald, 2017), and space debris capture and removal missions (Shan, Guo, & Gill, 2016). In such missions, an important capability to possess is the ability to safely, robustly and autonomously rendezvous and dock with spacecrafts in orbit.

The need for the development of advanced space GNC Verification and Validation (V&V) methods for extensive testing on Earth, before deployment in Space, is well recognized in the space community (Dennehy et al., 2024). Replicating high-fidelity three-dimensional zero gravity conditions on earth for GNC V&V is challenging and expensive. Three degree-of-freedom (3DOF) planar floating platforms fill this need and play a crucial role in incremental advancement of

* Corresponding author.
E-mail address: akshit.saradagi@ltu.se (A. Saradagi).

https://doi.org/10.1016/j.conengprac.2025.106274
Received 31 July 2024; Received in revised form 10 December 2024; Accepted 1 February 2025
Available online 17 February 2025

technology readiness levels (TRLs) and V&V of a wide range of in-plane orbital operations, as they emulate in-plane motion of spacecrafts under micro-gravity conditions on Earth (Rybus & Seweryn, 2016; Trentlage, Yang, Larbi, de Alba Padilla, & Stoll, 2018). Such platforms are economical alternatives to the costlier 6DOF emulators and are widely used, by both space industry and academia, for V&V of core GNC algorithms (Sabatini, Farnocchia, & Palmerini, 2012; Trentlage et al., 2018).

In this article, we present and experimentally validate a novel safe and autonomous docking strategy, designed for a planar floating platform depicted in Fig. 1 and referred to as Slider in the rest of the article (Banerjee et al., 2022; Gasparetto et al., 2021a). The Slider is a Hardware-in-loop (HIL) test-bed facility that has been designed to emulate the in-plane zero-gravity motion of a spacecraft, for the validation of emerging GNC algorithms. The Slider platform is supported by three air bearings, which release compressed air to form an air cushion (order of micro-meters in thickness) that allows Slider to levitate over a smooth surface. This air cushion provides frictionless translational and rotational motion on a relatively flat surface, thus emulating space-like zero-gravity conditions. More insights and details on the platform's design and operation are documented in Banerjee et al. (2022) and Sun, Li, Zhang, Lei, and Song (2022).

There are two main approaches to utilizing 3DOF floating platforms for V&V in space industry and academia. The top-down approach, where the core components of 6DOF GNC algorithms designed for in-plane orbital maneuvers are scaled down to be tested on 3DOF planar floating platforms. This approach is prevalent in space industries like ESA (Orbital Robotics Lab Bredenbeck, Vyas, Zwick, Borrmann, Olivares-Méndez, and Nüchter (2022)), JPL (Wapman, Sternberg, Lo, Wang, Jones-Wilson, and Mohan (2021)) etc., and is used to validate algorithms related to orbital satellite servicing, debris removal, human interaction with items in weightlessness, low gravity experiments and other operations that can make use of a controlled frictionless environment or simulated microgravity in two dimensions. The alternative bottom-up approach, used by industry and academia alike (El-Hariry, Richard, Muralidharan, Geist, & Olivares-Mendez, 2023; Huang, Zhang, Chen, Wen, & Jin, 2022; Kwok-Choon, Buchala, Blackwell, Lopresti, Wilde, & Go, 2018; Nieto-Peroy, Palmerini, de Oliveira, Gasbarri, Sabatini, & Milz, 2021), is more suited for the evaluation of the feasibility and TRL assessment of novel GNC technologies with potential for deployment in space, such as predictive collaborative controllers (Phodapol, Roque, & Dimarogonas, 2024), reinforcement learning-based spacecraft control (El-Hariry et al., 2023) etc.

In orbital space missions such as rendezvous and docking, in-plane maneuvers are preferred, as they are significantly less fuel-intensive than maneuvers requiring both in-plane and out-of-plane motion. For such applications, planar floating platforms provide near-ideal micro-gravity conditions and aid in accurate Hardware-in-the-loop testing of GNC algorithms. Several works in literature have effectively employed floating platforms (Rybus & Seweryn, 2016) to test novel docking mechanisms for orbital refueling (Sun et al., 2022), vision-based navigation (Huang et al., 2022), novel strategies for space manipulation (Sabatini, Gasbarri, & Palmerini, 2017), spacecraft rendezvous and robotic capture control (Santaguida & Zhu, 2023), satellite trajectory optimization and tracking (Bredenbeck et al., 2022), etc.

In this article, we pursue the bottom-up approach, to develop and evaluate a novel control barrier functions (CBFs)-based safe docking control strategy that caters to the in-plane approach and docking phases of space docking missions. The scenario where a Slider platform looks to dock with a docking station is shown in Fig. 1. Autonomous docking is a maneuver where deliberate contact is initiated between two entities, unlike a vast majority of robotics applications, where contact of any kind between the robot and the environment must be avoided. Given the narrow point of entry to the docking station (Fig. 1), the imposition of safe clearance constraint and direction of approach constraint is crucial in the design of docking control strategies. Moreover, the control design is expected to take into consideration non-ideal operating conditions, such as (i) disturbances induced by the tethering that supplies pressurized air to the air-bearings and thrusters, (ii) the non-flat floating surface, and (iii) the on–off nature of thruster firings, which are all extremely difficult to model. When docking with a narrow port, where precise contact has to be made, such uncertainties and unmodeled factors can be disastrous, especially for sensitive floating platforms.

Recently, works by Li, Yuan, Zhang and Wang (2019), Sun and Jiang (2020), Zhao and Zhang (2021) presented solutions to the space rendezvous and docking problem using constrained controllers. While controllers, such as in Sun and Jiang (2020), constrain the control inputs to account for actuator saturation, they neither generate a smooth docking maneuver nor impose state constraints to explicitly guarantee safety from collision with the target. The works by Zhao and Zhang (2021) and Li, et al. (2019) propose artificial potential field (APF) based state-constrained controllers. The parabolic APF used in Zhao and Zhang (2021) does not ensure collision avoidance or successful docking when the initial position of the Slider is outside the conical region in front of the docking station. Hence, controllers such as in Sun and Jiang (2020) and Zhao and Zhang (2021) are effective only for close-range rendezvous, when initialized in a region directly in front of the docking station. In this article, we present a robust and general docking solution that is applicable from a large set of initial conditions around the docking station. As in this article, the work by Li, et al. (2019) proposes an APF-based controller using a cardioid-shaped constraint set. Such a constraint naturally satisfies the two main requirements of collision avoidance with the docking station and accessibility of the docking station from the front to accomplish docking. Nevertheless, it is well-established that APF demands extensive tuning, without which it may induce oscillations, or result in the system converging to local minimas instead of configurations favorable for safe docking (Singletary et al., 2021).

In this article, we propose a control strategy based on the control barrier functions (CBF) approach, which has emerged in the recent years as an elegant framework for enforcing constraints in the state-space that ensure safety (Ames et al., 2019; Ames, Xu, Grizzle, & Tabuada, 2017). In this technique, barrier functions are constructed in such a way that their super-level sets capture configurations where the safety requirements are met. The super-level sets are then rendered robustly forward invariant throughout the execution of a control maneuver. In this work, we propose a switching strategy among the positive and zero level sets of a Cardioid CBF to enable safe and robust docking in the presence of unmodeled experimental non-idealities.

The CBF approach has been used to design docking strategies in Dunlap, Hibbard, Mote, and Hobbs (2022), Breeden and Panagou (2022) and in our earlier work (Saradagi, Banerjee, Satpute, & Nikolakopoulos, 2022), with the validation presented only in simulations. In Dunlap et al. (2022), distance-dependent velocity limits between the spacecraft and docking station and maximum velocity limits defined the barrier functions. In Breeden and Panagou (2022), the distance between the spacecraft and the docking station is taken into account in defining the barrier functions. The works mentioned so far, do not take into account crucial aspects, such as the design of the docking port and constraints associated with a specific direction of approach to a docking station. In our earlier work on CBF-based docking in Saradagi et al. (2022), such constraints in the proximity of the docking station were taken into account. In this article, a novel switched CBF-control strategy is proposed, by also taking into consideration the practical non-idealities of the experimental setup, to demonstrate robust docking for an experimental planar floating platform.

Contributions: (a) In this article, we present and experimentally validate a novel autonomous docking strategy, that is designed for an indigenously built experimental planar floating platform. The proposed switched CBF-based controller is computationally efficient and safely

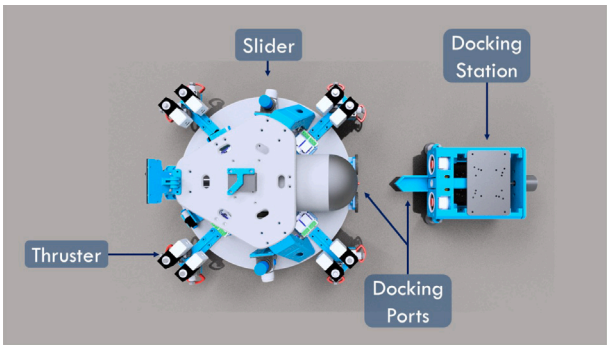

Fig. 1. A schematic of a docking scenario between the planar floating platform (Slider) on the left and a docking station with a narrow docking port on the right.

guides the Slider platform into the vicinity of the docking station (using the first CBF) and initiates the docking contact maneuver with a narrow docking port (using the second CBF). (b) Two contours of a cardioid function (positive contour and zero contour) are chosen as CBFs to incorporate the necessary clearance and direction-of-approach constraints with respect to the docking station. The condition for switching among the two CBFs leverages the deadlock scenario encountered in the implementation of the first CBF, at which the Slider attains a favorable configuration to initiate the docking contact. We present a precise characterization of the deadlock points of the Cardioid CBF and analyze their asymptotic stability properties. (c) Unlike the related works cited previously, this article presents experimental validation of the proposed docking strategy using a hardware-in-the-loop planar floating platform that levitates on a near-frictional table. (d) The experimental Slider platform deviates from the nominal model considered for control design, due to unmodeled factors such as non-flat floating surface, twists from the tether and on–off firing of the thrusters. A levitating platform is highly sensitive to such unmodeled factors and disturbances, especially when docking onto a narrow port, which demands high accuracy. We demonstrate that the proposed switched-CBF control strategy robustly handles such experimental non-idealities.

The rest of the article is organized as follows. In Section 2, we define the notations used in this work and recall important ideas related to CBFs. In Section 3, we present the dynamics of the Slider platform and derive CBFs that capture safety in the context of autonomous docking, while taking into consideration the practicalities and limitations of the experimental setup and the Slider platform. In Section 4, we derive the control barrier constraints and set up the Quadratic program that enforces the barrier constraints. Next, we derive a switching condition in Section 6, to switch the contours of the Cardioid when the Slider enters into a neighborhood of the deadlock point of the CBF filter. In Sections 8 and 9, we present the experimental setup and the experimental validation of the proposed docking strategy respectively, followed by concluding remarks in Section 10.

2. Notations and preliminaries

We denote the unit circle by $\mathbb{S}^1$. The notation $L_f h(x)$, is used to denote the Lie derivative of a continuously differentiable function $h(x)$ along the vector field $f(x)$, that is, $\frac{\partial h(x)}{\partial x} f(x)$. The boundary of a set $\mathcal{S}$ is denoted as $\partial\mathcal{S}$. A continuous function $\alpha : (-b, a) \to (-\infty, \infty)$ is said to be an extended class-$\mathcal{K}$ function if $\alpha(0) = 0$ and it is strictly increasing.

Next, we recall some results concerning control barrier functions (CBFs) from the work of Ames et al. (2019, 2017), which will be used in this work to design a novel docking control strategy for the Slider platform, that ensures safety throughout the docking maneuver.

Consider a control-affine dynamical system

$$\dot{x} = f(x) + g(x)u, \quad x \in \mathcal{X} \subset \mathbb{R}^n, \quad u \in \mathcal{U} \subset \mathbb{R}^m \tag{1}$$

where f and g are Lipchitz continuous functions. Let $\mathcal{S} \subset \mathcal{X}$ be the region of the state-space, which is deemed as a safe region for the operation of (1). Let $h(x) : \mathcal{D} \subset \mathcal{X} \to \mathbb{R}$ be a continuously differentiable function, with $\mathcal{S} \subset \mathcal{D}$, such that $\mathcal{S} := \{x \in \mathcal{X} \mid h(x) \geq 0\}$, that is, $\mathcal{S}$ is a zero super-level set of the function $h(x)$. The set $\mathcal{S}$ is rendered safe if the control input to (1) ensures positive invariance of the set $\mathcal{S}$, that is, $x(t_0) \in \mathcal{S}$ implies $x(t) \in \mathcal{S}$ for all $t \geq t_0$. In addition, if the set $\mathcal{S}$ is rendered asymptotically stable, when the system is initialized in $\mathcal{D} \setminus \mathcal{S}$, a measure of robustness can be incorporated into the notion of safety.

The following definition introduces the notion of a control barrier function and presents a condition, the verification of which, enables the design of a controller that renders the set $\mathcal{S}$ positively invariant and asymptotically stable and in turn ensures the safety of the dynamical system (1).

Definition 1 (*A Control Barrier Function (Ames et al., 2019)*)**.** A continuously differentiable function $h(x) : \mathcal{D} \to \mathbb{R}$ is a control barrier function, if there exists a real parameter $k > 0$ and an extended class-$\mathcal{K}$ function α, such that for all $x \in \mathcal{D}$,

$$\begin{aligned} &\sup_{u \in \mathcal{U}} \left\{ \dot{h}(x) + k\alpha(h(x)) \right\} \\ &\quad = \sup_{u \in \mathcal{U}} \left\{ L_f h(x) + L_g h(x) u + k\alpha(h(x)) \right\} \geq 0. \end{aligned} \tag{2}$$

The forward invariance of the set $\mathcal{S}$ ($\dot{h} \geq 0$ on $\partial\mathcal{S}$) and asymptotic stability of the set $\mathcal{S}$ ($\dot{h} > 0$ in $\mathcal{D} \setminus \mathcal{S}$) are captured together by the condition (2) in one-shot. If there exists at least one input in the admissible control input set $\mathcal{U}$ for every $x \in \mathcal{D}$, which renders the condition (2) feasible, then a controller can be designed to ensure safety of the dynamical system (1). In this article, two functions $h_1(x)$ and $h_2(x)$ will be presented in Section 4.2, which are valid control barrier functions for the Slider system and satisfy the condition set in Definition 1.

3. Problem formulation

In this section, we present the dynamics of the Slider platform, define safety in the context of autonomous docking and derive the control barrier functions, whose super-level sets capture the safe operating set, while taking into consideration the practical aspects of the experimental setup and control implementation.

3.1. Space rendezvous and docking missions

The autonomous space rendezvous and docking missions are split into two phases:

(i) The out-of-plane maneuvers, where the spacecraft aligns its orbit with the orbit of the docking station by tilting its inclination. This brings the spacecraft roughly in the same plane as the docking station. The out-of-plane maneuvers are costly in terms of fuel consumption and are performed a long time before the spacecraft approaches a docking station, which makes the subsequent maneuvers simpler and fuel-efficient.

(ii) Once the orbits of the spacecraft and the docking station are aligned, the in-plane rendezvous and docking maneuver begins, which comprises of three sub-stages: (a) phasing, where the spacecraft gains or loses velocity to adjust the relative orbital position to prepare for approaching the docking station, (b) the approach phase, where the spacecraft approaches and aligns with the docking port of the docking station and (c) docking phase, where the spacecraft moves to docks with the docking station using various interlocking mechanisms. The in-plane maneuvers are significantly more fuel-efficient than out-of-plane maneuvers.

In this article, the primary focus is on designing and validating a novel in-plane GNC docking strategy using the control barrier functions approach, which has gained popularity in systems and control research, but not yet looked into by the space research community. The design of the docking strategy primarily focuses on the in-plane (3DOF) approach and docking phases of real space docking missions.

3.2. Dynamics of the slider platform

The equations governing the motion of the Slider platform (derived in Banerjee et al. (2022)) in the state-space form are:

$$\begin{bmatrix} \dot{r}_x \\ \dot{r}_y \\ \dot{\theta} \\ \dot{v}_x^b \\ \dot{v}_y^b \\ \dot{\omega}_z \end{bmatrix} = \begin{bmatrix} v_x^b \cos\theta - v_y^b \sin\theta \\ v_x^b \sin\theta + v_y^b \cos\theta \\ \omega_z \\ \omega_z v_y^b + \frac{1}{m} f_x \\ -\omega_z v_x^b + \frac{1}{m} f_y \\ \frac{\tau_z}{I_{zz}} \end{bmatrix} \tag{3}$$

where, $r_x, r_y \in \mathbb{R}$ describe the position of the Slider with respect to the inertial frame. The angle $\theta \in \mathbb{S}^1$ represents the orientation of the Slider with respect to the inertial frame. The linear velocities $v_x^b, v_y^b \in \mathbb{R}$ and the rotational velocity $\omega_z \in \mathbb{R}$ are defined in the body-frame of the platform. The state of the Slider $x = (r_x, r_y, \theta, v_x^b, v_y^b, \omega_z)$ evolves in $\mathcal{Q}_1 = \mathbb{R}^5 \times \mathbb{S}^1$. The forces applied to the Slider in the body frame are denoted by f_x and f_y. The torque applied to the Slider is denoted by $\tau_z \in \mathbb{R}$ and $I_{zz} \in \mathbb{R}$ denotes the principal moment-of-inertia. The platform has been designed such that the other components of the moment of inertia matrix are negligible. The mass of the platform is denoted by m. The Coriolis effects influencing the motion of the Slider feature in the dynamics through the terms $\omega_z v_y$ and $-\omega_z v_x$.

Eq. (3) represents the nominal model of the Slider platform. The experimental platform (shown in Fig. 7 in Section 8), is designed such that the on–off thrusters on the robot are powered by a pressurized air-tank (a cylindrical tank on Slider shown in Fig. 1). However, the capacity of the tank does not suffice for continuous, extensive experimentation and the experimental setup uses an external tether (seen in Fig. 7) to supply the pressurized air. The twists in the tether introduce unmodeled dynamics and disturbances, which have significant effect on a levitating platform like the Slider. Moreover, the surface on which Slider levitates is not perfectly flat, due to which the Slider platform suffers from drifts along the gradient of the surface. Both these effects are hard to model and in this work, we look to design a docking control strategy that is designed on the nominal ideal model (Eq. (3)), but is robust to the two kinds of disturbances described above.

Remark 1. In this remark, we highlight the relationship between the Slider's 3DOF dynamics and the general 6DOF dynamic models considered in space research for spacecraft rendezvous and docking. (r_x, r_y, r_z), capturing the relative position of the spacecraft with respect to the docking station in the Local-Vertical Local-Horizontal (LVLH) frame and (θ, ϕ, ψ) capturing the attitude of the spacecraft constitute the six degrees-of-freedom. The relative dynamics between the spacecraft and the docking station for circular orbits is given by the Clohessy–Wiltshire (CW) Equation (Pesce, Colagrossi, & Silvestrini, 2022; Schaub & Junkins, 2018) which is presented next.

$$\begin{aligned} \ddot{r}_x - 2n\dot{r}_y - 3n^2 r_x &= u_x, \\ \ddot{r}_y + 2n\dot{r}_x &= u_y, \\ \ddot{r}_z + n^2 r_z &= u_z. \end{aligned} \tag{4}$$

Here, (r_x, r_y) constitutes the in-plane coordinates and r_z constitutes the out-of-plane coordinate. u_x, u_y, u_z are the control accelerations in the radial, along-track, and cross-track directions, respectively. n is a constant defined by the gravitational parameters and the orbital radius of the docking station.

The 3DOF rotational dynamics of the spacecraft concerning (θ, ϕ, ψ) are modeled separately and are decoupled from the relative translational dynamics. Moreover, notice that the in-plane (r_x, r_y) dynamics is decoupled from the out-of-plane r_z dynamics. When the orbital plane of both the spacecraft and the docking station match, $r_z \simeq 0$.

For the design of in-plane maneuvers, (r_x, r_y) and θ, the orientation within the plane, are relevant. The 3DOF second order dynamics of the Slider platform (presented in Eq. (3)) are qualitatively similar to the reduced in-plane dynamics of a spacecraft given by the CW Equation in Eq. (4).

The two-stage cascade control architecture, to be presented in Section 4, with the CBF-filter designed over the kinematics and the feedback linearization-based velocity tracking control, immediately applies to the reduced in-plane CW equations.

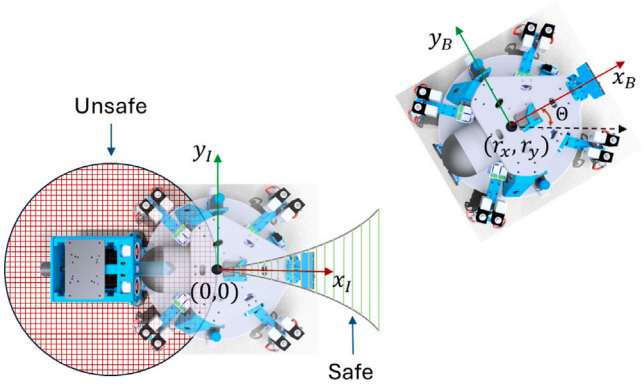

Fig. 2. The area around the docking station, indicated in red, is considered unsafe. The area inside the tapering funnel, indicated in green, is considered a safe region to approach the docking port. The inertial frame-of-reference and the body frame-of-reference fixed to the center of the slider are also shown. (For interpretation of the references to color in this figure legend, the reader is referred to the web version of this article.)

3.3. Safety constraints in autonomous docking

In a safe docking maneuver, the Slider is expected to approach the docking port of a docking station asymptotically, with the Slider's docking port aligned perfectly with that of the docking station. If the Slider blindly tracks the docking port on the docking station, there is a possibility of the Slider crashing into the docking station. This necessitates the definition of an unsafe clearance zone around the docking port and the imposition of direction-of-approach constraints with respect to the docking port on the docking station.

In Fig. 2, the two main constraints involved in autonomous docking are illustrated, along with the inertial and body frames-of-reference and the coordinates defining the position and orientation of the Slider platform. The origin of the inertial frame-of-reference is at the center of the Slider platform, when it is in the perfect docking state. The safe and the unsafe sets around the docking station are defined with respect to the center of the Slider platform in the docking state. We identify a region around the docking station (indicated in red, in Fig. 2) into

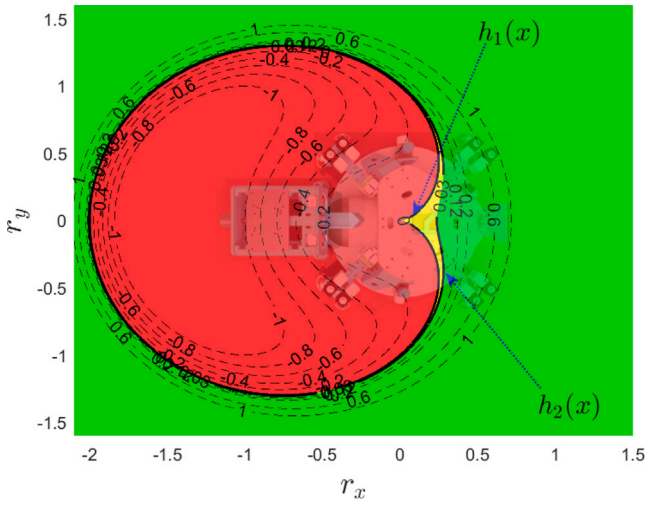

Fig. 3. The contours of a Cardioid function. The origin of the coordinate system coincides with the center of the Slider platform, when the two docking ports are perfectly interlocked. Both the safety and the direction-of-approach constraints are captured in one shot, by considering the area outside (inside) the Cardioid to be safe (unsafe). However, for practical implementations, the area outside a positive contour of a Cardioid (in this case 0.03 contour) is chosen to be the safe zone, to safely guide the Slider platform into the vicinity of the docking port.

which the Slider must be prohibited from entering. It is also expected that Slider approaches the docking port through a tapering funnel, shown in green in Fig. 2, while maintaining perfect alignment between the two ports. This is crucial when approaching a narrow docking port, as misalignment can lead to collision with the docking port, thus demanding high accuracy.

In Fig. 3, the contours of a Cardioid function, centered at the tip of the docking port and oriented along the positive r_x-axis, are shown. The Cardioid function is defined by

$$h_1(x) = (r_x^2 + r_y^2)^2 + 4ar_x(r_x^2 + r_y^2) - 4a^2r_y^2 = 0 \tag{5}$$

where a is a positive real parameter that decides the size of the Cardioid. The docking station is enclosed by the Cardioid. By defining the region outside (inside) the Cardioid as safe (unsafe), the safe clearance constraint, shown in red in Fig. 2, can be taken into account. The zero-contour of the Cardioid function has a cusp at the origin and acts as a tapering funnel, thus satisfying the direction-of-approach constraint indicated in green in Fig. 2. If it is ensured that the Slider remains outside the zero-contour of the Cardioid throughout the docking maneuver, we indirectly ensure in one shot, that both the safe clearance and the direction-of-approach constraints are satisfied.

In this work, we consider the Control Barrier Functions approach to impose state constraints, as this approach allows for systematic characterization of safe and unsafe zones for docking and results in an optimization-based control law which is computationally light (Section 4.3) in comparison with iterative trajectory reshaping. In this work, we look to address the problem of robust docking in the presence of unmodeled disturbances (without resorting to difficult modeling) and validation of the proposed strategy on an experimental floating platform. A novel contour switching strategy is proposed, that switches between the zero and positive level sets of a Cardioid function to enable precise interlocking between the docking ports, even in the presence of unmodeled disturbances.

4. Control architecture and CBFs for safe docking

In this section, we present a two-loop control architecture for the Slider platform and derive control barrier functions satisfying conditions in Definition 1, that establish the safety constraints introduced in the previous section.

4.1. Control architecture

We employ a two-loop control architecture for the Slider platform (shown in Fig. 4). The inner-loop has access to the inputs (forces f_x, f_y and torque τ_z) of the Slider and it is designed to track the inertial-frame velocities $\{v_x^d, v_y^d, \omega_z^d\}$ commanded by the outer-loop. In designing the inner-loop controller, feedback linearization is used first to negate the nonlinearities in the Slider dynamics (3) and then a linear controller is imposed to track the velocities commanded by the outer-loop. The controller

$$\begin{aligned} f_x &= m(-v_y^b\omega_z + c_1(v_x - v_x^d) + \dot{v}_x^d) \\ f_y &= m(v_x^b\omega_z + c_2(v_y - v_y^d) + \dot{v}_y^d) \\ \tau_z &= I_{zz}(c_3(\omega_z - \omega_z^d) + \dot{\omega}_z^d) \end{aligned} \tag{6}$$

where (v_x, v_y) are the velocities in the inertial frame, drives the errors $e_{v_x} = (v_x - v_x^d)$, $e_{v_y} = (v_y - v_y^d)$ and $e_{\omega_z} = (\omega_z - \omega_z^d)$ exponentially to zero and the positive constants c_1, c_2 and c_3 are chosen to achieve the desired rates of convergence. The vector $\{v_x, v_y, \omega_z\}$ is treated as input for designing the outer-loop

$$\begin{bmatrix} \dot{r}_x \\ \dot{r}_y \\ \dot{\theta} \end{bmatrix} = \begin{bmatrix} v_x \\ v_y \\ \omega_z \end{bmatrix}, \quad \begin{bmatrix} v_x \\ v_y \end{bmatrix} = \begin{bmatrix} v_x^b\cos\theta - v_y^b\sin\theta \\ v_x^b\sin\theta + v_y^b\cos\theta \end{bmatrix} \tag{7}$$

where $(r_x, r_y, \theta) \in \mathcal{Q}_2 = \mathbb{R}^2 \times \mathbb{S}^1$. We base our control strategy for safe autonomous docking on the kinematic model (7), with $\{v_x, v_y, \omega_z\}$ as the inputs, which are used to set command velocities (v_x^d, v_y^d, ω^d) for the inner-loop. Under the assumption that the magnitudes of the linear and angular velocities that can be faithfully tracked by the inner-loop are bounded by $a > 0$ and $b > 0$ respectively, the admissible control input set for the outer-loop is considered to be $\mathcal{U} = [-a\ \ a]\times[-a\ \ a]\times[-b\ \ b] \subset \mathbb{R}^3$.

4.2. Contours of the cardioid as barrier functions for safety

To impose the safety and direction-of-approach constraints around the docking port, as described in Section 3.3, we employ the zero and the positive level sets of the Cardioid function

$$h_1(x) = (r_x^2 + r_y^2)^2 + 4ar_x(r_x^2 + r_y^2) - 4a^2r_y^2 \tag{8}$$

$$h_2(x) = (r_x^2 + r_y^2)^2 + 4ar_x(r_x^2 + r_y^2) - 4a^2r_y^2 - c,\ c > 0 \tag{9}$$

with $\mathcal{H}_1 = \{x \in \mathcal{Q}_2 \mid h_1(x) \geq 0\}$ and $\mathcal{H}_2 = \{x \in \mathcal{Q}_2 \mid h_2(x) \geq 0 \equiv h_1(x) \geq c\}$ defining the corresponding safe sets. The negative, zero and positive level sets of a Cardioid function are shown in Fig. 3.

In our earlier work (Saradagi et al., 2022), only the zero-contour of the Cardioid function was considered as a control barrier function and simulation-based validation of safe docking was presented. In the experimental scenario however, this strategy was found to be fragile, as the Slider platform is subjected to tether-induced twists and drift-forces from the non-flat floating surface. Making precise docking contact and interlocking with the narrow docking port is the most crucial phase of the docking maneuver and the strategy proposed in Saradagi et al. (2022) was unsuccessful in experiments. When the attitude of the Slider is disturbed by unmodeled factors in the vicinity of the narrow docking port, the Slider entered unrecoverable configurations and the two docking ports failed to interlock.

In the presence of disturbances induced by the tether, directly initiating the docking contact maneuver is not advised. This observation leads us to propose a novel switched-CBF control strategy in this article, where we split the task of safe autonomous docking into two stages:

(1) *Safe guidance into close proximity of the docking station*: In guiding the Slider safely into the proximity of the docking station, the region outside a positive contour of the Cardioid, parameterized by the positive constant c, was found to be suitable for defining the safe zone. Considering the dimensions of the experimental setup (Slider and the docking station), the parameters a and c were chosen to be 0.5 and

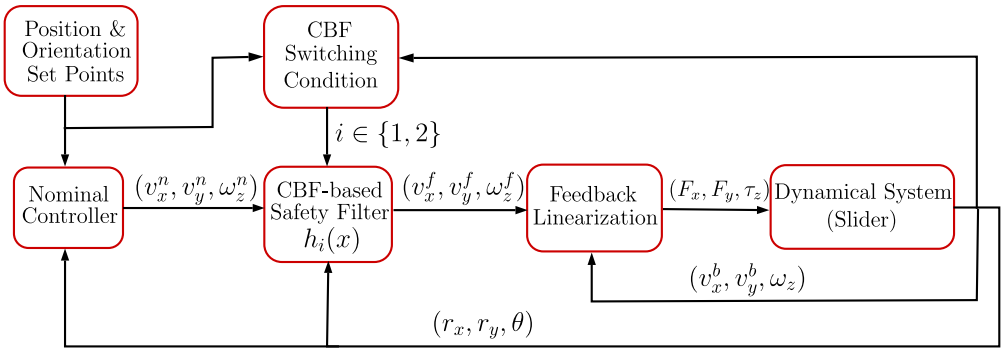

Fig. 4. Two-loop control architecture for the Slider platform. The inner-loop consists of a velocity-tracking controller based on feedback-linearization. The outer-loop consists of a kinematics-based nominal controller along with a CBF-based safety filter.

0.03 respectively. The safe zone defined by the CBF $h_2(x)$ is shown in green in Fig. 3. The extra clearance region over the nominal clearance provided by the function $h_1(x)$, is shown in yellow in Fig. 3. The size of the extra-clearance region is proportional to the positive parameter c, as can be seen from the contours in Fig. 3.

(2) *Robust and precise interlocking between docking ports*. The second stage is extremely crucial due to the narrow interlocking mechanism (shown in Fig. 1) used for docking. In close proximity of the docking port (while being in the green zone), only when the Slider reaches configurations favorable for smooth docking, the CBF can be switched to the zero contour, thus releasing the yellow zone between the zero and positive contours in Fig. 3, to be included into the safe zone. The docking contact and interlocking maneuver are initiated in this manner. This idea motivates the design of the contour switching strategy presented in Section 6.

In showing that $h_1(x)$ and $h_2(x)$ are valid control barrier function and satisfy the condition in Definition 1, the existence of the constants $k_i > 0$ and class$-\mathcal{K}$ functions α_i, such that

$$\begin{aligned}\sup_{u\in\mathcal{U}}\{L_f h_i(x) + L_g h_i(x)u\} &= \sup_{u\in\mathcal{U}}\{a_{11}v_x + a_{12}v_y + a_{13}\omega_z\}\\ &\geq -k_i\alpha_i(h_i(x)),\quad i\in\{1,2\}\end{aligned} \tag{10}$$

where

$$\begin{aligned}a_{11} &= \frac{\partial h_1}{\partial r_x} = -(4(r_x^2+r_y^2)r_x + 4a(r_x^2+r_y^2) + 8ar_x^2)\\ a_{12} &= \frac{\partial h_1}{\partial r_y} = -(4(r_x^2+r_y^2)r_y + 8ar_xr_y - 8a^2r_y)\\ a_{13} &= \frac{\partial h_1}{\partial \theta} = 0\end{aligned} \tag{11}$$

is feasible in a set $\mathcal{D}_i \supset \mathcal{H}_i$ must be shown. This was established for the zero-contour of the cardioid, through the proofs presented in our previous work (Saradagi et al., 2022). As the proof for the positive contour of the Cardioid follows along similar lines, we do not include it in this article. Note that, as the positive constant c is the only difference between the two CBFs, the state-dependent parameters $a_{11} - a_{13}$ are the same for both CBFs.

4.3. CBF-based quadratic program for safety guarantees

In the CBF approach, a control filter is designed, which takes a nominal controller $u_{\text{nom}}(x)$ as input and yields a minimally deviating filtered control input $u^*(x)$ that enforces the safety constraint (10) and ensures safety as defined by the CBFs. In this work, we use a linear proportional–integral controller $u_{\text{nom}}(x(t)) = [-p_1 r_x(t) - p_1^a\int_0^t r_x(t)dt \quad -p_2 r_y(t) - p_2^a\int_0^t r_y(t)dt \quad -p_3\theta(t) - p_3^a\int_0^t \theta(t)dt]^\top$, with the gains $p_i, p_i^a > 0$, as the nominal controller for the Slider kinematics (7). This simple nominal controller has been designed with no consideration for the safety constraints, and exponentially drives the Slider to the origin of the (r_x, r_y) plane, with its docking port aligned with the docking port on the docking station. The CBF approach takes such a nominal controller and filters it to yield the controller $u^*(x)$ that ensures positive invariance of the safe zone.

As the functions $h_i(x)$ are CBFs, for a fixed x, the constraints (10) are feasible linear constraints in the control vector u. The filtered control $u^*(x) = (v_x^f, v_y^f, \omega_z)$ is derived by solving the following minimum-norm Quadratic program

$$\begin{aligned}u^*(x) &= \arg\min_{u\in\mathcal{U}} ||u - u_{\text{nom}}(x)||^2\\ \text{subject to}\ &:\ L_f h_i(x) + L_g h_i(x)u \geq -k_1\alpha(h_i(x)),\end{aligned} \tag{12}$$

where $i \in \{1,2\}$ is chosen by the switching condition (14) (in Section 6) to appropriately select one among $h_1(x)$ and $h_2(x)$ at any point in time.

The classical Quadratic program (12) with the quadratic cost and linear constraints in the decision variable $u = \{v_x, v_y, \omega_z\}$ can be efficiently solved at every sampling instant. When the controller $u^*(x)$ is Lipschitz continuous, the forward invariance of the sets $\mathcal{H}_1$ and $\mathcal{H}_2$ and their asymptotic stability from the corresponding sets $\mathcal{D}_1 \setminus \mathcal{H}_1$ and $\mathcal{D}_2 \setminus \mathcal{H}_2$ (as described in Section 2) can be established using Comparison Lemma (as in Ames et al. (2019) and Orosz and Ames (2019)).

Next, we present the notion of 'Deadlock Point' of a CBF filter and determine the deadlock configurations that are asymptotically reached by the Slider platform when using the CBF $h_2(x)$. Then, we present a switching mechanism that switches the barrier functions in the CBF filter from $h_2(x)$ to $h_1(x)$ when the Slider reaches configurations that are favorable to initiate the docking contact maneuver.

5. Deadlock points of the CBF filter

The nominal controller $u_{\text{nom}}(x)$ is designed to achieve the configuration $r_x = r_y = \theta = 0$ asymptotically. When this nominal controller is passed through the CBF filter (12) with $h_2(x)$ as the CBF, at two points where $h_2(x)$ cuts the r_x-axis, the CBF filter returns $u^*(x) = 0$ even though $u_{\text{nom}}(x) \neq 0$. This is due to the unresolvable conflict between the nominal controller's objective of reaching the origin (in the unsafe zone as defined by the CBF $h_2(x)$) and the CBF filter's objective of restricting the state outside the c-contour of the Cardioid. Such points are called deadlock points and we denote this set of points by

$$\mathcal{D}_l = \{x \in \mathcal{D} \mid u_{\text{nom}}(x) \neq 0 \text{ and } u^*(x) = 0\}. \tag{13}$$

Next, we analyze the CBF filter in Eq. (12) to (i) provide an interpretation for how the CBF filter transforms $u_{\text{nom}}(x)$ to $u^*(x)$ and to (ii) present a detailed characterization of the deadlock points of CBF $h_2(x)$. For simplicity of analysis, we consider a proportional controller $u_{\text{nom}}(x) = [-p_1 r_x \quad -p_2 r_y \quad -p_3\theta]^\top$ as the nominal controller. In Figs. 5(a) and 5(b), the admissible control set $\mathbb{U}$ is shown as a green box; the feasible control set $\mathcal{F}(x) \subseteq \mathbb{U}$, beyond the tangent at the point x in the direction of $\frac{\partial h}{\partial x}$, is indicated by the black arrows; and the nominal control input $u_{\text{nom}}(x)$ is shown through a purple arrow, at two illustrative locations on the boundary of the CBF $h_2(x)$.

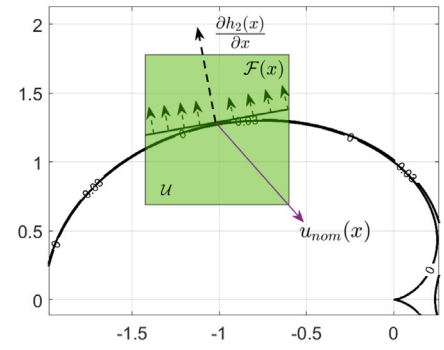

(a) $h_2(x) = 0$ and $x = 1$.

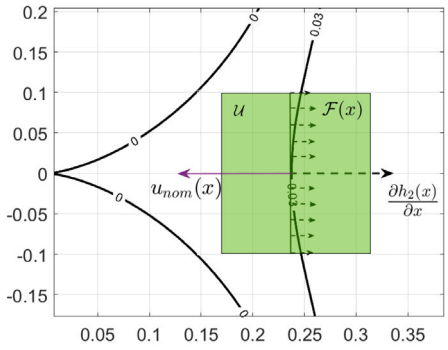

(b) $h_2(x) = 0$ and $y = 0$.

Fig. 5. Illustration of the functioning of the CBF filter at different points on the contour $h_2(x) = 0$. In case (a), a non-deadlock point is considered, while in case (b), a deadlock point is considered.

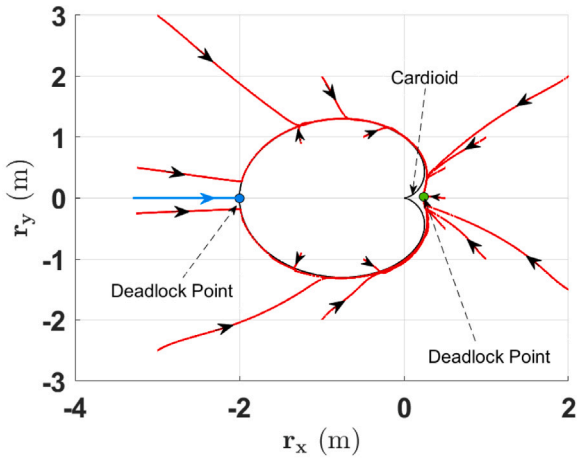

(a) The trajectories of the closed-loop system (7)-(12) asymptotically converge to the deadlock point d (shown as a green dot). The other deadlock point $\bar{d}$ is an unstable point of the closed-loop system.

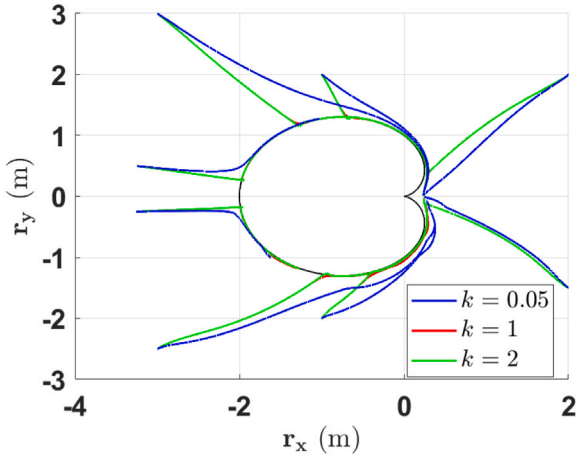

(b) The influence of the design parameter k from Equation (2) on the trajectories of the close-loop system (7)-(12).

Fig. 6. The trajectories of the closed-loop system (7)–(12) from various initial conditions, for different choices of the design parameter k from Eq. (2).

$\mathcal{F}(x)$ denotes the set of feasible control inputs in the optimization problem (12) at $x \in D$, i.e, $\mathcal{F}(x) = \{u \in \mathbb{U} \mid \dot{h}_2 \geq k\alpha(h_2(x))\}$. On the boundary of $h_2(x)$, $\mathcal{F}(x) = \{u \in \mathbb{U} \mid \dot{h}_2(x) = \frac{\partial h}{\partial x}\dot{x} = \frac{\partial h}{\partial x}u \geq 0\}$, as $h_2(x) = 0$ on the boundary. As the optimization problem minimizes $||u - u_{\text{nom}}(x)||$, the output of the CBF filter $u^*(x)$ is the projection of $u_{\text{nom}}(x)$ onto the set $\mathcal{F}(x)$.

With this interpretation in place, the deadlock points satisfying the definition in Eq. (13) are configurations at which the projection of $u_{\text{nom}}(x)$ onto the set $\mathcal{F}(x)$ is the zero vector, i.e $D_l = \{x \in D \mid u_{\text{nom}}(x) - (\partial\hat{h}_2^\top u_{\text{nom}}(x))\partial\hat{h}_2 = 0\}$, where $\partial\hat{h}_2$ is the unit vector along the gradient of the function $h_2(x)$ at x. In Fig. 5(a), the point defined by $h_2(x) = 0$ and $x = 1$ is considered, which is not a deadlock point as both $u_{\text{nom}}(x) \neq 0$ and $u^*(x) \neq 0$. In Fig. 5(b), the point defined by $h_2(x) = 0$ and $y = 0$ is considered, which is a deadlock point as $u_{\text{nom}}(x) \neq 0$ but $u^*(x) = 0$. For the CBF $h_2(x)$, the set $\mathcal{D}_l = \{d = (x_1, 0, 0), \bar{d} = (x_2, 0, 0)\}$, which consists of two points where the function $h_2(x)$ cuts the r_x-axis and the scalars x_1 and x_2 are the real roots of the equation $r_x^4 + 4ar_x^3 - c = 0$. The two deadlock points are shown in Fig. 6(a) as blue and green dots.

Most often in CBF literature (especially in multi-agent settings) the CBF-based control design is such that deadlock points are avoided. In this work, we specifically exploit a deadlock point of the CBF $h_2(x)$ to safely guide the Slider to a safe point in the vicinity of the docking station. The value of the contour c is chosen such that the deadlock point is at a desired safe distance from the docking port. Under the CBF implementation, the deadlock point d is an asymptotically stable equilibrium point of the closed-loop system (7)–(12), i.e, when the Slider is initialized from the feasible region of the CBF filter, from the set $D \setminus (\bar{S} \cup \{\bar{d}\})$, the Slider asymptotically converges to the deadlock point d with the docking port of the Slider aligned with the docking port of the docking station. In Fig. 6(a), we present the trajectories of the closed-loop system (7)–(12) from various initial conditions in the feasible region of the CBF filter. It can be seen that the deadlock point d is asymptotically stable from the feasible zone. On the other hand, the deadlock point $\bar{d}$ is an unstable point, as the only trajectories that converge to $\bar{d}$ begin from points on the r_x-axis with $r_x \leq -2$. One such trajectory is indicated in blue in Fig. 6(a). In Fig. 6(b), we show the effect of the design parameter k_i on the trajectories of the closed-loop system (7)–(12). As the parameter k is increased, the trajectories tend to the c-contour of the Cardioid and asymptotically reach the deadlock point d along the c-contour. For smaller values of k, the trajectories asymptotically tend to the deadlock point d, but the tendency to quickly tend to the c-contour of the Cardioid is reduced.

6. Switching between contours of the Cardioid

In this section, we exploit the deadlock point of the CBF $h_2(x)$ to design a practical and robust switching methodology that expands the safe zone for the Slider platform by switching the barrier function in the CBF filter (12) from $h_2(x)$ to $h_1(x)$.

We propose the following switching condition:

$$x \in S_w = \{x \in D \mid h_1(x) < (c + \gamma), |\theta| < \delta_\theta \text{ and } |r_y| < \delta_y\} \tag{14}$$

The switching condition (14) effectively identifies a neighborhood of the deadlock point where $h_1(x) < (c + \gamma)$ or equivalently $h_2(x) < \gamma$, the

attitude of Slider is close to the attitude desired for smooth docking (parameterized by δ_θ) and the Slider has close alignment with the docking port along the r_y-axis (parameterized by δ_y). The conditions in the set definition (14) are satisfied when Slider is in the vicinity of the deadlock point and its attitude is favorably positioned to initiate docking. The funnel-shaped region (shown in yellow in Fig. 7), which was unsafe when $h_2(x)$ was active, becomes part of the safe region when $h_1(x)$ is activated, thus initiating the docking contact maneuver.

The switching condition (14) is continually checked and on encountering violations due to tethering-induced disturbances or drifts induced by the non-flat floating surface, the barrier function is switched back to $h_2(x)$, which removes the yellow zone from the safe region and the Slider is pushed away from the docking port. This is due to the asymptotic attractivity to $\mathcal{H}_2$ encoded in the barrier constraint (10) of the CBF filter.

Remark 2. In the presence of persistent and large disturbances, there is a risk of chattering, or the switching signal swinging back and forth. However, this would pose a challenge for any other method, unless there is a disturbance estimator providing accurate disturbance forecasts. In the proposed method, the switching condition is designed to ensure that the robot configuration is apt for a smooth docking contact maneuver. As will be seen in the experimental results, in the presence of tether-induced disturbances, the robot docks successfully after a few switches.

Remark 3. In the proposed approach, there is no a priori design of a trajectory for docking. The nominal controller (a feedback controller for position tracking) + CBF filter combination generates references for the Slider platform on-the-go, while respecting the safety constraints captured by the Cardioid. A competing approach to the problem of robust docking is through the design of a fixed trajectory that satisfies all the safety constraints and using an accurate trajectory tracking controller to track the designed trajectory. However, in the presence of external disturbances close to the docking port, the transients involved in recovering from disturbances would lead to unsuccessful docking. Online trajectory reshaping is computationally expensive and does not guarantee successful docking, as it does not take into account unknown future disturbances.

7. Extension to 6DOF operations

The Slider's 3DOF dynamics in (r_x, r_y, θ) captures the complexities involved in the design of in-plane orbital maneuvers.

Over the 3DOF in-plane dynamics considered in this article, the stability along the remaining three DOF (r_z, ϕ, ψ) is crucial. In real spacecraft control architectures, this is handled by additional stabilization controllers, which are designed independently. The decoupling between the (r_x, r_y) and r_z dynamics in the CW equation (Eq. (4)) for relative orbital dynamics and the decoupling of the attitude control design from the control of translational DOF allows for the independent design of the controllers. As the spacecraft performs in-plane maneuvers, stability in the out-of-plane r_z and (ϕ, ψ) DOF is handled by the corresponding controllers in the presence of disturbances and perturbations.

7.1. Scaling of the proposed approach to 3D operation

The scaling of the two main elements in the proposed docking strategy into three dimensions is necessary for 6DOF operations.

7.1.1. Formulation of the 3D safe set

In this work, we proposed a 2D Cardioid as the control barrier function. This is easily extended into a 3D Cardioid which captures the collision avoidance and direction-of-approach constraints in three dimensions. Since the definition of the safe set concerns only the translational degrees-of-freedom, the extension from 2D Cardioid to a 3D Cardioid suffices to translate the definition of safety into three dimensions.

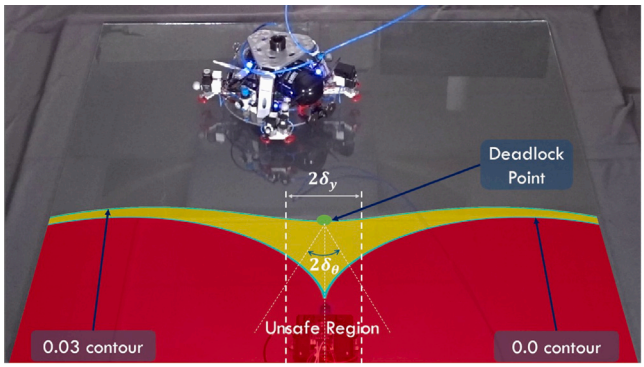

Fig. 7. Experimental Setup: The Slider levitates on a flat and smooth glass surface with dimensions of 1.5 m× 1.5 m. The docking port is located in the middle of the bottom edge of the table. Also illustrated is the deadlock point and the conditions for CBF switching from $h_2(x)$ to $h_1(x)$.

7.1.2. The CBF switching condition

In the vicinity of the deadlock point, this article presented a CBF switching condition (Eq. (14)) to enable a robust docking contact maneuver.

Taking the stability along the out-of-plane r_z DOF and the (ϕ, ψ) attitudes into account, the switching condition can be scaled for 3D operations in the following manner.

$$x \in S_w = \{x \in \mathcal{D} \,|h_1(x) < (c+\gamma), |\theta| < \delta_\theta, \;\; |\phi| < \delta_\phi, \\ |\psi| < \delta_\psi, \;\; |r_z| < \delta_z \;\text{ and }\; |r_y| < \delta_y\} \tag{15}$$

where, $h_1(x)$ is the 3D Cardioid. The above switching condition would govern the switching between the zero and positive level sets of the 3D cardioid to enable robust docking in the presence of disturbances.

7.2. Limitations of 2D floating platforms for comprehensive testing of 6DOF operations

Although planar floating platforms are used widely for extensive validation of in-plane orbital maneuvers, extensive simultaneous validation of in-plane, out-of-plane and attitude stabilizing controllers is necessary and this constitutes a limitation of planar floating platforms. Validation of 6DOF operation in high-fidelity three-dimensional microgravity conditions requires expensive testing facilities such as those available with major space agencies. Moreover, real spacecraft and satellites models have to be scaled down for hardware-in-the-loop testing in a limited area. Both the bottom-up and top-down approaches to the design and validation of GNC algorithms using 2D floating platforms are complemented with extensive 3D simulations to test the robustness of the overall GNC strategy in three dimensions.

8. Experimental setup

To demonstrate the effectiveness of the proposed docking strategy and its robustness to unmodeled dynamics and disturbances introduced by the tether and the non-flat floating surface, several experimental trials were conducted. The experimental setup is shown in Fig. 7.

The Slider platform levitates over a smooth flat table of size 1.5 m × 1.5 m, using the air cushion provided by the air bearings. The footprint of the Slider robot, which is approximately 0.25 m × 0.25 m, is significant in comparison to the flat table and this presents a limitation on the set of configurations from which the Slider can be initialized. The docking port is placed in the middle of the bottom edge of the table, to provide a large set of initial conditions from the first and the fourth quadrants of the Slider's operating space. More details about the design of the docking port can be found in Gasparetto et al. (2021b). We present a more complete validation of the proposed strategy through

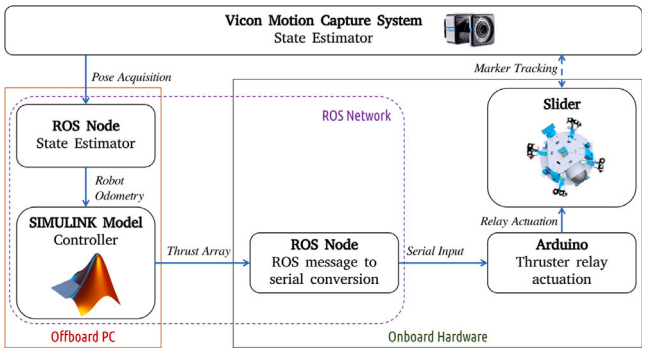

Fig. 8. A block diagram of closed-loop implementation of the proposed docking control strategy, with ROS implementation details and the integration of the experimental setup with the motion capture system.

simulations in Figs. 6(a) and 6(b), where we plot the trajectories of the robot from several initial conditions and present the effect of the CBF filter parameter k on the trajectories of the closed-loop system.

In Fig. 8, we present a block diagram of the closed-loop control implementation, with ROS implementation details and the integration of the experimental setup with the motion capture system, which provides state estimates for the proposed docking control strategy. A 12-camera Vicon motion capture system (MCS) is used to localize the Slider. The localization messages from the MCS are processed by a state estimator to obtain the pose and velocities of the Slider. The control architecture presented in Section 4.1 has been implemented in MathWorks-SIMULINK. The controller and the state estimator run on an off-board computer with a 3.50 GhZ processor and 16 GB RAM. The controller provides the thrust messages as Pulse-Width-Modulated (PWM) ON/OFF commands to the onboard computer. A ROS network is established over the WiFi for the controller to communicate with the state-estimator and transmit the control messages to the onboard computer. The ROS toolbox in SIMULINK is used to subscribe and publish the ROS messages. The Slider Platform is equipped with a Single-Board-Computer (SBC) Up-Board UP-CHT01, equipped with a QuadCore Intel Atom x5-z8350 Processor and 4 GB DDR3L-1600 memory running a Linux-based OS. The onboard computer receives the thrust PWMs over the ROS network and converts them into serial messages for the low-level Microcontroller (Arduino) to enable/disable the thruster relays at a sampling frequency of 10 Hz.

9. Experimental results

In the experimental results presented in this Section, the parameters of the Slider platform are $m = 4.82$ kg and $I_{zz} = 0.11$ kg m^2. The upper and lower bounds on the thrust that can be generated by the thrusters are $T_h^{\max} = 0.7\,\text{N}, T_h^{\min} = 0$ N respectively. The thrusters are on–off thrusters with a minimum on-time of $t_{on}^{min} = 0.05$ s.

The design parameter a defining the Cardioid is chosen to be 0.5 m. The 0.0 and 0.03 contours of the Cardioid function are chosen as barrier functions to implement the switching methodology presented in 6. In the switching condition (14), the parameter $\gamma = 0.002$, $\delta_\theta = 5\pi/180$ rad and $\delta_y = 0.04$m. We use the parameters $k_i = 1$ and $\alpha_i(x) = x^3$ in the barrier constraints of the Quadratic program (12). The admissible control set $\mathcal{U} = [-0.5 \quad 0.5]^3$ restricts the magnitude of the linear velocities and the angular velocities to within 0.5 m/s and 0.5 rad/s respectively. The gains c_i in the inner-loop controller (6) are chosen to be $c_1 = c_2 = 1.5$ and $c_3 = 1.5$. The gains of the proportional–integral nominal outer-loop controller in Section 4.3 are chosen to be $p_1 = p_2 = 0.15$, $p_1^a = p_2^a = 0.01$, $p_3 = 0.25$ and $p_3^a = 0.025$.

In Fig. 9, we present the experimental results obtained using the docking control strategy proposed in this work. We present results from three initial conditions, picked from the two quadrants of the planar

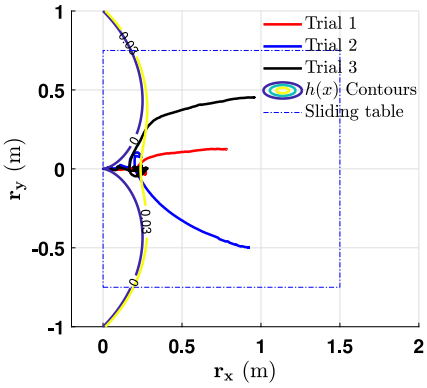

(a) The Slider platform achieves safe autonomous docking from three initial conditions.

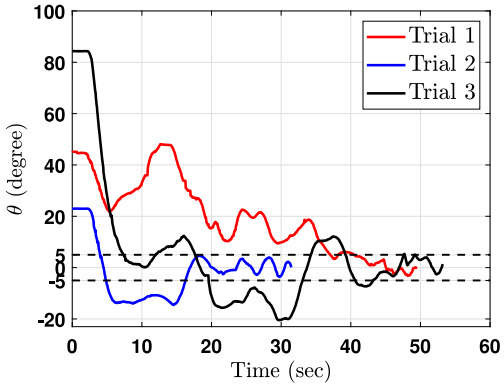

(b) The evolution of the attitude of the Slider platform indicates that the Slider reaches the docking port with θ in a small neighborhood of zero.

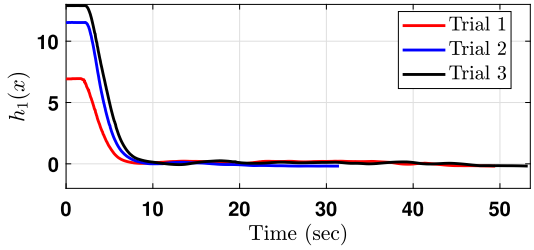

(c) The CBF $h_1(x)$ is maintained positive throughout the docking maneuver and tends to zero with time.

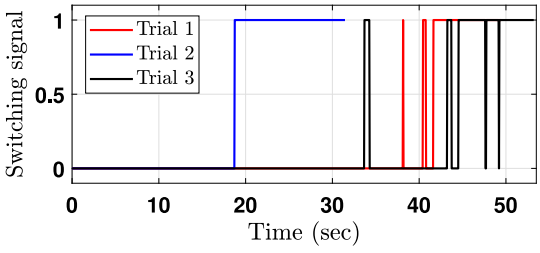

(d) The CBF switching signal from the three experimental trials.

Fig. 9. Experimental results from three trials, showing successful docking and the positive invariance of the safe set throughout the docking maneuver.

space from which the Slider can be initialized within the limitations of the experimental setup. In Fig. 9(a), the two contours of the Cardioid functions are plotted along with the evolution of the position of the Slider in three experimental trials. The boundary of the 1.5 m × 1.5 m sliding surface is shown using a blue dash-dot square. In all the three trials, the Slider approaches the deadlock point of the 0.03 contour of the cardioid and adjusts its configuration until the switching

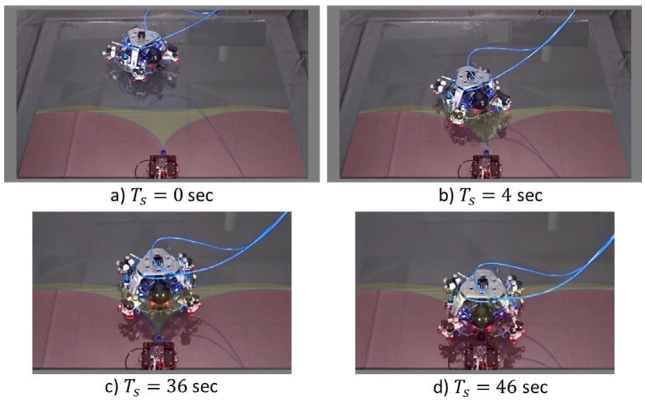

Fig. 10. Snapshots from the first experimental trial, with the data presented in Fig. 9. (a) The Slider is initialized on the floating surface. (b) The Slider is guided to the vicinity of the deadlock point by CBF $h_2(x)$. (c) The Sliders corrects its position and attitude until the switching condition in Eq. (14) are satisfied. (d) The CBF is switched from $h_2(x)$ to $h_1(x)$ and the docking contact maneuver is initiated and the Slider docks successfully.

condition (14) is satisfied. When the switching condition is satisfied, the space between the two contours is released to be included into the safe zone and the docking contact maneuver is initialized. We see that the disturbances from the tether lead to the switching conditions being violated, which pushes the Slider away from the docking port. This is manifested as temporary oscillations in the neighborhood of the deadlock point, following which the Slider successfully achieves docking. In Fig. 9(b), we plot the evolution of the heading angle of the Slider. We see that the attitude of the Slider tends to zero, but with small oscillations (contained within 5 degrees) as it makes contact with the docking port.

In Fig. 9(c), we see that the barrier function $h_1(x)$ remains positive throughout the docking maneuver and tends to zero with time, which implies safe and successful docking. After successful docking, the ports on the robot and the docking station get interlocked and in the final stages, the robot pushes firmly into the docking station leading to the function $h_1(x)$ going slightly negative, as can be seen in Fig. 9(c).

In Fig. 9(d), we plot the CBF switching signal for the three experimental trials. The switch from zero to one indicates the switching of the barrier functions from $h_2(x)$ to $h_1(x)$, which initiates the docking contact. In Trial 1 and Trial 3 we see that there are several instances where the disturbances act after the CBF has been switched from $h_2(x)$ to $h_1(x)$ (when space in the proximity of the docking port has been released). This leads to the violation of condition (14) and the CBF is switched back from the zero contour $h_1(x)$ to the positive contour $h_2(x)$. This results in the robot being pushed away from the docking port, which in turn gives time for the robot to correct its configurations to meet the requirements in the switching condition (14). This repeats until successful docking is completed, post which the switching signal is held at one. In Trial 1 and Trial 3 successful docking is achieved after 5 and 4 attempts respectively. In Trial 2, no such switching was found to be necessary, as there were no major disturbances after the CBF was switched from $h_2(x)$ to $h_1(x)$.

In Fig. 10, four snapshots from Trial 1, illustrating the different phases in a successful docking maneuver are shown. A video of experimental demonstrations can be found at: https://youtu.be/eBiWvnKtG7U?si=QFPD-vm11wydyZSd.

10. Conclusions

In this article, we presented and experimentally validated a novel safe and autonomous docking strategy for a Planar Floating Platform, called the Slider. The control strategy was based on the control barrier functions approach, where a nominal controller is passed through a Quadratic programming-based CBF safety filter that enforces the safety constraints. A positive contour of the Cardioid function was used to safely steer the Slider to configurations around a deadlock point, following which the barrier function is switched to expand the safe region and initiate the docking contact maneuver. The switching strategy resulted in robust docking, even when the Slider entered unfavorable docking configurations due to tethering-induced disturbances and drifts induced by the non-flat floating surface. Experimental results were presented to validate the effectiveness of the proposed approach. As part of our future work, we look to upgrade the experimental setup (so that docking from a larger set of initial conditions can be demonstrated) and tetherless operation, which is more representative of space-like zero-gravity operation.

Funding

None declared. The research presented in this article is not supported by any funding agency.

CRediT authorship contribution statement

Akshit Saradagi: Writing – review & editing, Writing – original draft, Visualization, Validation, Methodology, Investigation, Formal analysis, Data curation, Conceptualization. **Viswa Narayanan Sankaranarayanan:** Writing – review & editing, Validation, Methodology. **Avijit Banerjee:** Writing – review & editing, Supervision, Investigation, Conceptualization. **Sumeet Satpute:** Writing – review & editing, Supervision, Investigation, Conceptualization. **George Nikolakopoulos:** Writing – review & editing, Supervision, Methodology, Investigation, Conceptualization.

Declaration of competing interest

The authors declare that they have no known competing financial interests or personal relationships that could have appeared to influence the work reported in this paper.

Appendix A. Supplementary data

Supplementary material related to this article can be found online at https://doi.org/10.1016/j.conengprac.2025.106274.

References

Ames, A. D., Coogan, S., Egerstedt, M., Notomista, G., Sreenath, K., & Tabuada, P. (2019). Control barrier functions: Theory and applications. In *2019 18th European control conference* (pp. 3420–3431). http://dx.doi.org/10.23919/ECC.2019.8796030.

Ames, A. D., Xu, X., Grizzle, J. W., & Tabuada, P. (2017). Control barrier function based quadratic programs for safety critical systems. *IEEE Transactions on Automatic Control*, *62*(8), 3861–3876. http://dx.doi.org/10.1109/TAC.2016.2638961.

Banerjee, A., Satpute, S. G., Kanellakis, C., Tevetzidis, I., Haluska, J., Bodin, P., et al. (2022). On the design, modeling and experimental verification of a floating satellite platform. *IEEE Robotics and Automation Letters*, *7*(2), 1364–1371. http://dx.doi.org/10.1109/LRA.2021.3140134.

Barbara, N. H., Lizy-Destrez, S., Guardabasso, P., & Alary, D. (2020). New GEO paradigm: Re-purposing satellite components from the GEO graveyard. *Acta Astronautica*, *173*, 155–163.

Bredenbeck, A., Vyas, S., Zwick, M., Borrmann, D., Olivares-Méndez, M. A., & Nüchter, A. (2022). Trajectory optimization and following for a three degrees of freedom overactuated floating platform. In *2022 IEEE/RSJ international conference on intelligent robots and systems* (pp. 4084–4091). URL: https://api.semanticscholar.org/CorpusID:250331087.

Breeden, J., & Panagou, D. (2022). Guaranteed safe spacecraft docking with control barrier functions. *IEEE Control Systems Letters*, *6*, 2000–2005. http://dx.doi.org/10.1109/LCSYS.2021.3136813.

Dennehy, C., Bennani, S., Shankar, U., Vandersteen, J., VanZwieten, T., Von der Porten, P., et al. (2024). Verification and validation (v&v) of guidance & control systems: results from the first inter-agency workshop on GNC v&v. In M. Sandnas, D. B. Spencer (Eds.), *Proceedings of the 44th annual American astronautical society guidance, navigation, and control conference, 2022* (pp. 399–432). Cham: Springer International Publishing.

Dunlap, K., Hibbard, M., Mote, M., & Hobbs, K. (2022). Comparing run time assurance approaches for safe spacecraft docking. *IEEE Control Systems Letters*, *6*, 1849–1854. http://dx.doi.org/10.1109/LCSYS.2021.3135260.

El-Hariry, M., Richard, A., Muralidharan, V., Geist, M., & Olivares-Mendez, M. (2023). Drift: Deep reinforcement learning for intelligent floating platforms trajectories. arXiv preprint arXiv:2310.04266.

Gasparetto, T., Banerjee, A., Tevetzidis, I., Haluska, J., Kanellakis, C., & Nikolakopoulos, G. (2021a). Design of docking mechanism for refueling free-flying 2D planar robot. In *2021 aerial robotic systems physically interacting with the environment* (pp. 1–8). http://dx.doi.org/10.1109/AIRPHARO52252.2021.9571050.

Gasparetto, T., Banerjee, A., Tevetzidis, I., Haluska, J., Kanellakis, C., & Nikolakopoulos, G. (2021b). Design of docking mechanism for refueling free-flying 2D planar robot. In *2021 aerial robotic systems physically interacting with the environment* (pp. 1–8). http://dx.doi.org/10.1109/AIRPHARO52252.2021.9571050.

Huang, Z., Zhang, W., Chen, T., Wen, H., & Jin, D. (2022). Characterizing an air-bearing testbed for simulating spacecraft dynamics and control. *Aerospace*, *9*(5), http://dx.doi.org/10.3390/aerospace9050246, URL: https://www.mdpi.com/2226-4310/9/5/246.

Kwok-Choon, S. T., Buchala, K., Blackwell, B., Lopresti, S. E., Wilde, M., & Go, T. H. (2018). Design , fabrication , and preliminary testing of air-bearing test vehicles for the study of autonomous satellite maneuvers. URL: https://api.semanticscholar.org/CorpusID:195780984.

Li, W.-J., Cheng, D.-Y., Liu, X.-G., Wang, Y.-B., Shi, W.-H., Tang, Z.-X., et al. (2019). On-orbit service (OOS) of spacecraft: A review of engineering developments. *Progress in Aerospace Sciences*, *108*, 32–120.

Li, Q., Yuan, J., Zhang, B., & Wang, H. (2019). Artificial potential field based robust adaptive control for spacecraft rendezvous and docking under motion constraint. *ISA Transactions*, *95*, 173–184.

Nieto-Peroy, C., Palmerini, G., de Oliveira, E. J., Gasbarri, P., Sabatini, M., & Milz, M. (2021). Simulation of spacecraft formation maneuvers by means of floating platforms. In *2021 IEEE aerospace conference (50100)* (pp. 1–10). http://dx.doi.org/10.1109/AERO50100.2021.9438537.

Orosz, G., & Ames, A. D. (2019). Safety functionals for time delay systems. In *2019 American control conference* (pp. 4374–4379). http://dx.doi.org/10.23919/ACC.2019.8814681.

Pesce, V., Colagrossi, A., & Silvestrini, S. (2022). *Modern spacecraft guidance, navigation, and control: from system modeling to AI and innovative applications*. Elsevier.

Phodapol, S., Roque, P., & Dimarogonas, D. V. (2024). Collaborative load transportation in microgravity environments: Centralized and decentralized predictive controllers. In *2024 IEEE 20th international conference on automation science and engineering* (pp. 1548–1553). http://dx.doi.org/10.1109/CASE59546.2024.10711680.

Roa Garzon, M. A., Nottensteiner, K., Wedler, A., & Grunwald, G. (2017). Robotic technologies for in-space assembly operations. In *14th symposium on advanced space technologies in robotics and automation*. URL: https://elib.dlr.de/116805/.

Rybus, T., & Seweryn, K. (2016). Planar air-bearing microgravity simulators: Review of applications, existing solutions and design parameters. *Acta Astronautica*, *120*, 239–259. http://dx.doi.org/10.1016/j.actaastro.2015.12.018, URL: https://www.sciencedirect.com/science/article/pii/S0094576515004634.

Sabatini, M., Farnocchia, M., & Palmerini, G. B. (2012). Design and tests of a frictionless 2D platform for studying space navigation and control subsystems. In *2012 IEEE aerospace conference* (pp. 1–12). IEEE.

Sabatini, M., Gasbarri, P., & Palmerini, G. B. (2017). Coordinated control of a space manipulator tested by means of an air bearing free floating platform. *Acta Astronautica*, *139*, 296–305. http://dx.doi.org/10.1016/j.actaastro.2017.07.015, URL: https://www.sciencedirect.com/science/article/pii/S0094576517302680.

Santaguida, L., & Zhu, Z. H. (2023). Development of air-bearing microgravity testbed for autonomous spacecraft rendezvous and robotic capture control of a free-floating target. *Acta Astronautica*, *203*, 319–328. http://dx.doi.org/10.1016/j.actaastro.2022.11.056, URL: https://www.sciencedirect.com/science/article/pii/S0094576522006725.

Saradagi, A., Banerjee, A., Satpute, S., & Nikolakopoulos, G. (2022). Safe autonomous docking maneuvers for a floating platform based on input sharing control barrier functions. In *2022 IEEE 61st conference on decision and control* (pp. 3746–3753). http://dx.doi.org/10.1109/CDC51059.2022.9993109.

Schaub, H., & Junkins, J. L. (2018). *Analytical mechanics of space systems* (4th ed). AIAA.

Shan, M., Guo, J., & Gill, E. (2016). Review and comparison of active space debris capturing and removal methods. *Progress in Aerospace Sciences*, *80*, 18–32.

Singletary, A., Klingebiel, K., Bourne, J., Browning, A., Tokumaru, P., & Ames, A. (2021). Comparative analysis of control barrier functions and artificial potential fields for obstacle avoidance. In *2021 IEEE/RSJ international conference on intelligent robots and systems* (pp. 8129–8136). IEEE.

Sun, L., & Jiang, J. (2020). Saturated adaptive relative motion coordination of docking ports in space close-range rendezvous. *IEEE Transactions on Aerospace and Electronic Systems*, *56*(6), 4889–4898.

Sun, Z., Li, S., Zhang, H., Lei, H., & Song, X. (2022). Design and analysis of a novel floating docking mechanism for on-orbit refueling. *Aerospace*, *9*(7), http://dx.doi.org/10.3390/aerospace9070365, URL: https://www.mdpi.com/2226-4310/9/7/365.

Trentlage, C., Yang, J., Larbi, M. B., de Alba Padilla, C., & Stoll, E. (2018). The ELISSA laboratory: Free-floating satellites for space-related research. In *Deutscher luft-und raumfahrtkongress, Friedrichshafen, Germany*.

Wapman, J. D., Sternberg, D. C., Lo, K., Wang, M., Jones-Wilson, L. L., & Mohan, S. (2021). Jet propulsion laboratory small satellite dynamics testbed planar air-bearing propulsion system characterization. *Journal of Spacecraft and Rockets*, URL: https://api.semanticscholar.org/CorpusID:236598706.

Zhao, X., & Zhang, S. (2021). Adaptive saturated control for spacecraft rendezvous and docking under motion constraints. *Aerospace Science and Technology*, *114*, Article 106739.